PCCP

PAPER

View Article Online
View Journal | View Issue

Cite this: *Phys. Chem. Chem. Phys.*, 2016, **18**, 26049

Multiple-decker and ring sandwich formation of manganese–benzene organometallic cluster anions: $Mn_nBz_n^-$ (n = 1–5 and 18)†

Tsugunosuke Masubuchi,[a] Takeshi Iwasa[ab] and Atsushi Nakajima*[abc]

Received 3rd August 2016,
Accepted 1st September 2016

DOI: 10.1039/c6cp05380g

www.rsc.org/pccp

Organometallic multiple-decker sandwich clusters are topics of great interest due to their unique electronic and magnetic properties originating from anisotropic structures. We report a joint anion photoelectron spectroscopic and computational study on a new family of manganese (Mn)–benzene (Bz) anionic clusters $Mn_nBz_n^-$. In stark contrast to the most widely studied vanadium–Bz sandwich clusters, it is found that $Mn_nBz_n^-$ (n = 1–5) clusters exhibit unprecedented multiple-decker structures with a tilted Mn–Bz stacking and a monotonically increasing behavior of their high spin multiplicities. Furthermore, a couple of closed ring forms of $Mn_{18}Bz_{18}^-$ and its neutral state are computationally anticipated as an intriguing "cluster of Mn_1Bz_1 clusters" in which the neutral $Mn_{18}Bz_{18}$ has extremely high C_{18h} symmetry with an uncommon spin state of $2S + 1 = 55$. The extensively delocalized electron environment of $Mn_{18}Bz_{18}$ allows the simple Hückel model to reveal the strong intra-atomic exchange interactions within the Mn 3d electrons.

1. Introduction

Molecular magnetism has received considerable attention due to potential technological applications for high-density information storage,[1] quantum computing,[2] and molecular spintronics.[3,4] A variety of single-molecule magnets (SMMs), whose individual molecules act as a magnet, have been developed since the discovery of the first SMM, a manganese (Mn)–oxo cluster $[Mn_{12}]$.[5] Mn-based SMMs have been most investigated due to the significant contribution of Mn electrons to their spin states and magnetic anisotropy.[6] More recently, one-dimensional (1D) polymer chains called single-chain magnets (SCMs) have been demonstrated to show magnetic properties analogous to those of SMMs.[7,8] They can be viewed as 1D systems composed of high-spin magnetic units when compared with 0D SMMs.

A popular approach towards making better performing SMMs/SCMs is to realize a high-spin ground state with a large magnetic anisotropy. Major progress in this direction has been often made through appropriate modulation of existing systems. For example, a strategic choice of bridging ligands has been demonstrated to induce effective exchange interactions with a large anisotropy in the metal–ligand system.[9–12] On the other hand, their local electronic structures have to be characterized not only to understand their molecular magnetism but also to gain a concept for future SMM/SCM developments. At this point, there are several fruitful contributions from the field of cluster research.[13–16] They have shown that clusters are appropriate models for nanoscale magnetism, which can be described as a function of cluster size.

Clusters are also expected as a potential building block for designer SMMs/SCMs. Organometallic sandwich clusters are topics of great interest due to their unique electronic and magnetic properties originating from anisotropic structures.[17,18] For example, vanadium (V) atoms and benzene (Bz) molecules are piled up alternately to form multiple-decker sandwich structures (V_nBz_m; $m = n - 1$, n, and $n + 1$),[19] exhibiting a monotonic increase in their magnetic moments with increasing number of sandwich layers.[20,21] While this observation has stimulated numerous theoretical attempts to explore metal–ligand sandwich based SMM/SCMs,[22–26] experimental approaches remain challenging.

Here we report the size-dependent geometric and electronic structures on a new class of Mn–Bz cluster anions, $Mn_nBz_n^-$ (n = 1–5 and 18), by means of anion photoelectron spectroscopy in combined with theoretical calculations. We first show experimental and theoretical evidences of multiple-decker formation for $Mn_nBz_n^-$ (n = 1–5) through quite different stacking forms that

[a] *Department of Chemistry, Faculty of Science and Technology, Keio University, 3-14-1 Hiyoshi, Kohoku-ku, Yokohama 223-8522, Japan. E-mail: nakajima@chem.keio.ac.jp*
[b] *JST, ERATO, Nakajima Designer Nanocluster Assembly Project, 3-2-1 Sakado, Takatsu-ku, Kawasaki 213-0012, Japan*
[c] *Keio Institute of Pure and Applied Sciences (KiPAS), Keio University, 3-14-1, Hiyoshi, Kohoku-ku, Yokohama 223-8522, Japan*

† Electronic supplementary information (ESI) available: Full citation of ref. 32, computational details, additional photoelectron spectra of $Mn_nBz_n^-$ (n = 1–5), all optimized structures for $Mn_nBz_n^-$ (n = 1–5), Kohn–Sham orbital energy levels of Mn_nBz_n (n = 1 and 18) and [18]annulene, cohesive energies of $Mn_nBz_n^-$ (n = 1–5 and 18), comparison of calculations employing different DFT functionals, and Cartesian coordinates. See DOI: 10.1039/c6cp05380g

contrast with the linear V–Bz clusters. Then we computationally investigate extremely high-spin ring $Mn_{18}Bz_{18}^{-/0}$ clusters, whose motifs can intriguingly be recognized as a "cluster of Mn_1Bz_1 clusters".

2. Experimental and computational methods

2.1 Experimental methods

$Mn_nBz_m^-$ clusters were generated in the gas phase using a laser vaporization and supersonic expansion method.[27,28] Briefly, a Mn metal rod sample was ablated with the second harmonic (532 nm) light pulses of a Nd^{3+}:YAG laser at a 10 Hz repetition rate. The Mn vapor was reacted with helium-diluted Bz gas (at ~3 atm) that was introduced using a pulsed valve (General Valve Series 9), and then very intense supersonic pulses of helium carrier gas at 40 atm, obtained by using a high-pressure Even–Lavie pulsed valve,[29] were used to cool the hot species mixture of atoms and clusters. The resulting cluster anions were then extracted to a linear time-of-flight mass spectrometer. The anions were mass-selected and photodetached using the second (532 nm, 2.33 eV), third (355 nm, 3.49 eV), and fourth (266 nm, 4.66 eV) harmonic outputs of another Nd^{3+}:YAG laser. The kinetic energies of the detached photoelectrons were measured using a magnetic bottle-type photoelectron spectrometer. The electron binding energies were then obtained using the energy-conservation relationship $h\nu$ = EBE + EKE, where $h\nu$, EBE, and EKE are the photon energy, electron binding energy, and electron kinetic energy, respectively.

2.2 Computational methods

In order to explore the structures of Mn–Bz clusters, density functional theory (DFT) calculations were performed at the unrestricted BP86[30,31] level, implemented in the Gaussian 09 program package[32] using the def2-TZVP[33] basis sets. The Molekel program[34] was used for molecular visualization. The vertical detachment energies (VDEs) of each of the optimized anions were calculated to compare with the experimental values. Details of the computational method are provided in the ESI.†

It is important to correctly evaluate the energy orderings of different spin states of $Mn_nBz_n^-$ clusters, as it has been pointed out that the current DFT methods for transition metal-based organometallic systems have a specific problem that the spin multiplicity of a global-minimum structure depends on the functional employed.[35] In this study, $Mn_1Bz_1^{-/0}$ were optimized using various functionals to calculate the ADE/VDE values of $Mn_1Bz_1^-$, and the BP86 was adopted on the basis of the reasonable agreements with the experimental values (see Tables S2 and S3 in the ESI†).

3. Results and discussion

3.1 Mass distribution of $Mn_nBz_m^-$

Fig. 1 shows a typical mass spectrum of gas-phase produced $Mn_nBz_m^-$ cluster anions. It was taken by using a pulse duration

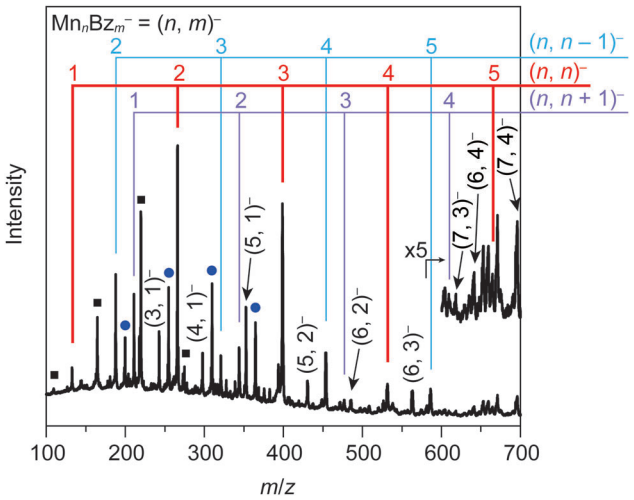

Fig. 1 Mass spectra of $Mn_nBz_m^-$. The peak assignments for $(n, m)^-$ = $(n, n-1)^-$, $(n, n)^-$, and $(n, n+1)^-$ are indicated with vertical lines. Several dominant $(n, m)^-$ clusters with $m \leq n-2$ are also labeled. Coexistent naked Mn_n^- clusters and incomplete Mn–Bz cluster anions are marked by ■ and ●, respectively.

of 280 μs for the Bz pulsed valve. Changes of the duration were found to significantly affect both the mass intensity and distribution (*vide infra*). The mass assignments were reconfirmed by the experiment using d_6-benzene (C_6D_6; see Fig. S1 in the ESI†). The spectrum indicates that various compositions of $Mn_nBz_m^-$ are generated; in particular, $Mn_nBz_n^-$ and $Mn_nBz_{n-1}^-$ are more intense than $Mn_nBz_{n+1}^-$ and the other $Mn_nBz_m^-$ with $m \leq n-2$. Other mass species are mostly classified into either pure Mn_n^- (marked by ■) or incomplete Mn–Bz cluster anions (marked by ●) which have a single Bz molecule and which cannot be assigned to $Mn_nBz_m^-$.

We assessed how the mass distribution is affected by kinetic conditions (*i.e.*, Bz introduction time) in the cluster source, which were qualitatively controlled by changing the duration of the Bz pulsed valve. Relative abundances of $Mn_nBz_m^-$ with different valve durations employed are depicted in Fig. 2, showing that the production of $Mn_nBz_m^-$ with large m (*e.g.*, $m = n$) is much more diminished by limiting the Bz introduction time than that of other Bz-poor $Mn_nBz_m^-$ ($Mn_1Bz_1^-$, $Mn_2Bz_1^-$, and $m \leq n-2$ for $n \geq 3$). In contrast, the mass distribution of the Bz-poor $Mn_nBz_m^-$ (for each n) is not shifted irrespective of the experimental conditions. Taken into account that the mass distribution of kinetically generated species must be controlled by the concentration of reactants,[36] these characteristics suggest that the production of most $Mn_nBz_m^-$ ($m = n-1$, n, and $n+1$) can be ruled by a kinetic process while the others (*i.e.*, $Mn_1Bz_1^-$, $Mn_2Bz_1^-$, and $m \leq n-2$ for $n \geq 3$) would experience a thermodynamic cluster growth. The difference in cluster growth mechanisms could also cause (co)existence of energetically higher structural isomers for some sizes of $Mn_nBz_n^-$, which is discussed in the following subsection.

The present study hereafter concentrates on the structural and electronic properties of $Mn_nBz_n^-$ (*i.e.*, $m = n$) according to their high abundances in the mass spectra.

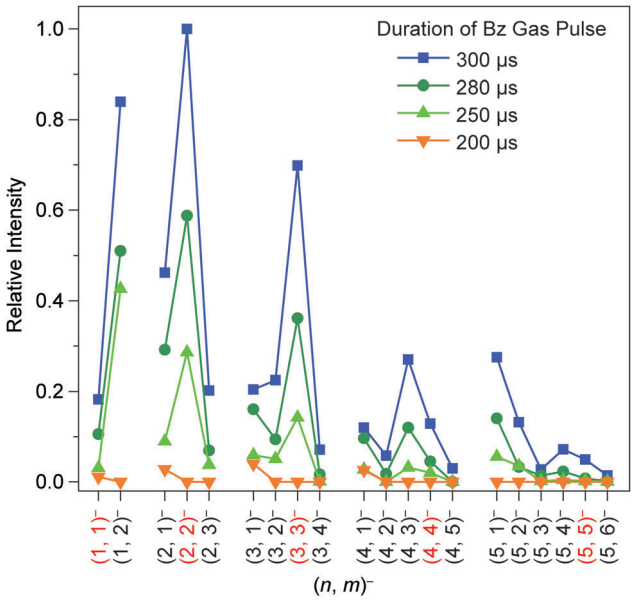

Fig. 2 Relative abundance of $Mn_nBz_m^-$ clusters with different conditions of the cluster generation source employed. Each $Mn_nBz_m^-$ is denoted as $(n, m)^-$. To guide the eyes, $Mn_nBz_n^-$ clusters are colored in red. The generation conditions were qualitatively controlled by changing the duration of the Bz pulsed valve. The average uncertainty on the vertical axis (estimated from the standard deviation) is ±20%. Note that the photoelectron spectra in the present study were measured under the condition of ≥280 μs unless otherwise noted.

3.2 Photoelectron spectra and structural assignments of $Mn_nBz_n^-$ (n = 1–3)

Fig. 3a shows the photoelectron spectra of $Mn_nBz_n^-$ (n = 1–3) taken with 355 nm radiation. The additional spectra measured with different wavelengths (532 nm and 266 nm; Fig. S2 in the ESI†) exhibit a photon energy-independent feature. Each peak maximum in the spectra provides VDE and the first VDEs of $Mn_1Bz_1^-$, $Mn_2Bz_2^-$, and $Mn_3Bz_3^-$ are defined from the 532 nm spectra as, respectively, 0.76 ± 0.02, 1.21 ± 0.02, and 1.11 ± 0.01 eV. In addition, higher VDEs of other spectral peaks are summarized in Table 1. The $Mn_1Bz_1^-$ spectrum has a vibrational feature with a spacing of 240 ± 40 cm^{-1} (inset of Fig. 3a), which is assignable to a stretching mode between Mn and Bz in the excited state of neutral Mn_1Bz_1. The first sharp peak of $Mn_1Bz_1^-$ also determines an adiabatic detachment energy (ADE) of 0.58 ± 0.07 eV, which reflects the electron affinity of Mn_1Bz_1.

Our DFT calculations found the most plausible structures for $Mn_nBz_n^-$ (n = 1–3) as depicted in Fig. 3b. The calculated VDEs of these structures are in good agreement with the experimental data (Fig. 3a and Table 1). $Mn_1Bz_1^-$ was identified as the quintet spin state having a C_{2v} (pseudo-C_{6v}) half-sandwich structure **1** (Fig. 3b). The other spin states are higher in energy and are ruled out due to inconsistency of VDEs (Table S3 in the ESI†). This observation of the lowest-lying **1** is in line with the thermodynamic behavior of $Mn_1Bz_1^-$ (Fig. 2). For neutral Mn_1Bz_1, the quartet state with perfect C_{6v} symmetry (Fig. S3 in the ESI†) was obtained and the calculated ADE of

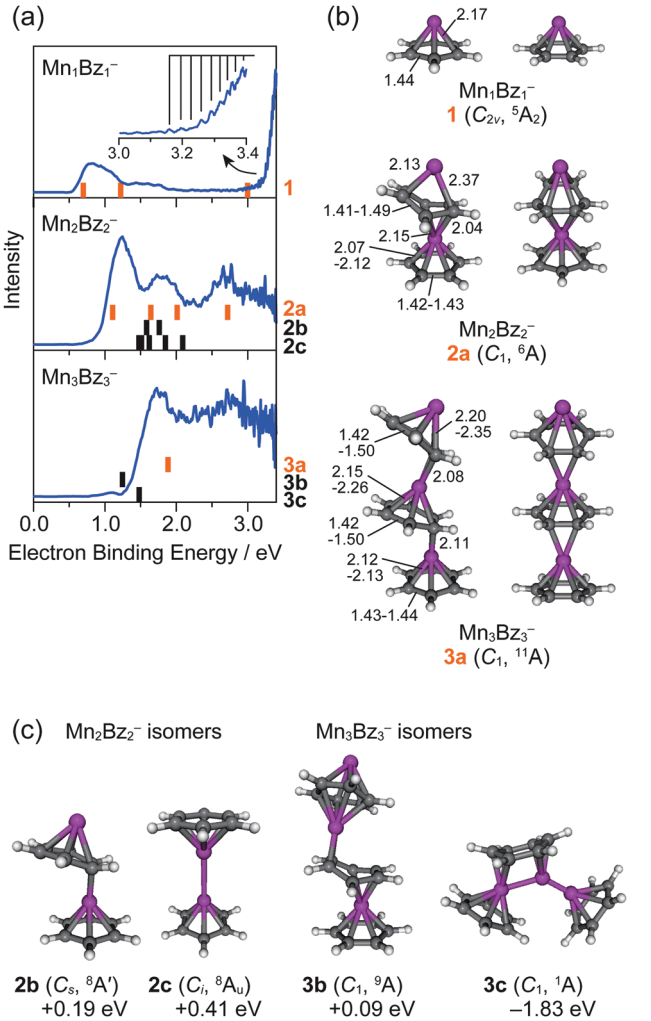

Fig. 3 (a) Photoelectron spectra of $Mn_nBz_n^-$ (n = 1–3) taken with 355 nm (3.49 eV) radiation. The calculated VDEs of the plausible structures are indicated below the spectra with vertical bars. Bold-faced labels right to the VDE bars are denoted to identify the structures. For $Mn_1Bz_1^-$, a vibrational progression is also shown. (b) Front and side views of the most plausible structures for each $Mn_nBz_n^-$ (n = 1–3) with their symmetries and electronic states. Typical bond lengths are indicated in Å. Bonds are visible for C–C, C–H, and Mn–C with distances of <2.4 Å only to guide the eyes. They do not necessarily represent single bonds. (c) Structural isomers with possible contributions to the photoelectron spectra and their symmetries, electronic states, and energies relative to **2a** ($Mn_2Bz_2^-$) and **3a** ($Mn_3Bz_3^-$).

$Mn_1Bz_1^-$ (0.59 eV) agrees well with the experimental value. Both the higher VDEs of 1.22 and 2.98 eV are ascribed to electronic excited states of the neutral Mn_1Bz_1.

Both $Mn_2Bz_2^-$ and $Mn_3Bz_3^-$ were identified as **2a** and **3a** (Fig. 3b), respectively. Both exhibit alternating sandwich structures with C_1 (pseudo-C_s) symmetry, where Mn atoms and Bz molecules are alternately stacked. They adopt relatively high spin states of $2S + 1$ = 6 (**2a**) and 11 (**3a**). Energetically closer **2b** and **3b** (Fig. 3c) might be minor products which contribute to the photoelectron spectra. Our extensive searches further found structural isomers (Fig. S4 and S5 as well as Tables S4 and S5, ESI†), some of which are even lower in energy than **2a** or **3a**.

Table 1 Experimental and calculated VDEs (in eV) for $Mn_nBz_n^-$ (n = 1–5)

Cluster	VDE	
	Expt.[a]	Calc.[b]
$Mn_1Bz_1^-$	0.76 ± 0.02	0.69 (**1** → $^4A_2$), 1.22 (**1** → $^6A_2$)
	3.47 ± 0.03[c]	2.98 (**1** → $^4A_1$)
$Mn_2Bz_2^-$	1.21 ± 0.02	1.10 (**2a** → ^5A)
	1.75 ± 0.07	1.47 (**2c** → ^9A_g), 1.51 (**2c** → ^9A_g), 1.58 (**2b** → $^7A'$), 1.62 (**2c** → ^9A_u), 1.64 (**2a** → ^7A), 1.76 (**2b** → $^9A'$), 1.85 (**2c** → ^9A_u), 2.01 (**2a** → ^7A), 2.09 (**2b** → ^7A_u)
	2.60 ± 0.06[d]	2.72 (**2a** → ^7A)
$Mn_3Bz_3^-$	1.11 ± 0.01	1.25 (**3b** → ^8A)
	1.75 ± 0.03	1.48 (**3c** → ^2A), 1.88 (**3a** → ^{10}A)
$Mn_4Bz_4^-$	2.16 ± 0.08	2.25 (**4** → ^{15}A)
$Mn_5Bz_5^-$	2.16 ± 0.07	2.24 (**5** → ^{18}A)

[a] Obtained from the 532 nm spectra (Fig. S2 in the ESI) unless otherwise noted because photoelectron resolution is better at smaller photon energies. [b] Labels of anions (Fig. 3b, c and 4b) and final electronic states are denoted in parentheses. For $n \geq 3$, higher VDEs (indicating excited final states) are not shown because several TD-DFT calculations met fatal problems such as "Fatal Problem: The smallest beta delta epsilon is 0.54335749D-03". [c] Obtained from the 266 nm spectra (Fig. S2 in the ESI). [d] Obtained from the 355 nm spectra.

However, the observation of the alternating sandwich structures will be reasonable if kinetic processes dominates their production. To confirm whether both **2a** and **3a** were kinetically produced, the photoelectron spectra of $Mn_2Bz_2^-$ and $Mn_3Bz_3^-$ were measured under a different kinetic condition. As shown in Fig. S6 in the ESI,† the limited introduction of Bz gas only diminishes the photoelectron features related to the alternating sandwiches (*i.e.*, **2a**, **2b**, **3a**, and **3b**). This change apparently corresponds the decreasing population of $Mn_2Bz_2^-$ and $Mn_3Bz_3^-$ shown in Fig. 2, thus affirming that $Mn_2Bz_2^-$ and $Mn_3Bz_3^-$ are mostly the kinetically generated alternating sandwich clusters. In contrast, the remaining spectral features at higher binding energies (>2 eV) indicate coexistence of structural isomers for both $Mn_2Bz_2^-$ and $Mn_3Bz_3^-$, which are determined as non-alternating structures **2c** and **3c** (Fig. 3c), respectively. In particular, **3c** is a so-called rice-ball cluster with a metal core surrounded by Bz molecules. It is generally concluded that such rice-ball clusters would become dominant under the thermodynamic conditions regarding Bz-poor (*e.g.*, n = 1) $Mn_nBz_m^-$, which are not capable of taking alternating sandwich structures due to smaller m ($< n - 1$).

3.3 Photoelectron spectra and structural assignments of $Mn_nBz_n^-$ (n = 4 and 5)

The photoelectron spectra of $Mn_4Bz_4^-$ and $Mn_5Bz_5^-$ are shown in Fig. 4a. The VDEs of $Mn_4Bz_4^-$ and $Mn_5Bz_5^-$ are determined to be 2.16 ± 0.08 and 2.16 ± 0.07 eV, respectively, according to the peak maxima of the broad features in the 532 nm spectra (Fig. S2 in the ESI†). As the kinetic generation is also the case for $Mn_4Bz_4^-$ and $Mn_5Bz_5^-$ (Fig. 2), we focus on the possibilities of multiple-decker sandwich structures. Assuming a monotonic increase of the $Mn_nBz_n^-$ spin multiplicities, the calculations found $Mn_4Bz_4^-$ (**4**) and $Mn_5Bz_5^-$ (**5**) with $2S + 1$ = 14 and 17, respectively, as depicted in Fig. 4b. It is noted that both **4** and **5**, in addition to **3a**, have an unprecedented "tilted" form, representing continuous η^2 binding of $Mn_1(\eta^6\text{-Bz})_1$ units. Both the calculated VDEs (Table 1 and Table S6 in the ESI†) are in line with the experimental values, showing the high spin-state multiple-decker formation of $Mn_4Bz_4^-$ and $Mn_5Bz_5^-$.

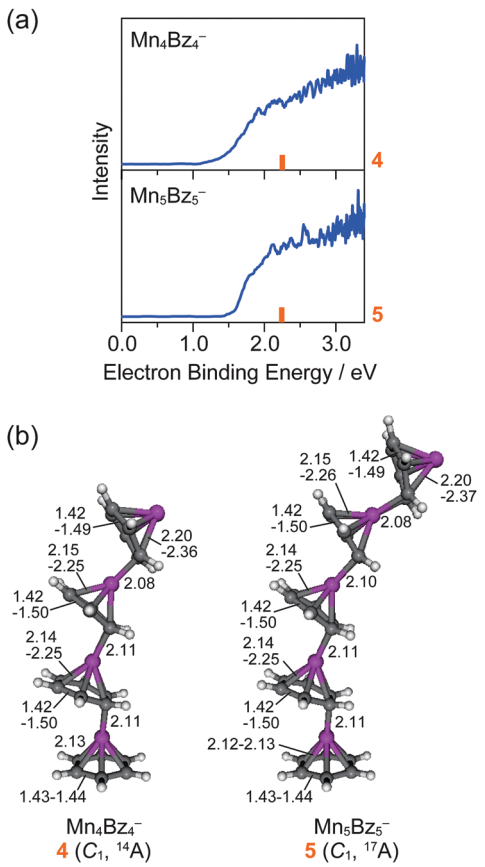

Fig. 4 (a) Photoelectron spectra of $Mn_4Bz_4^-$ and $Mn_5Bz_5^-$ taken with 355 nm (3.49 eV) radiation. (b) Optimized structures of $Mn_4Bz_4^-$ and $Mn_5Bz_5^-$ in a multiple-decker sandwich fashion, with their symmetries and electronic states. The indications are shown in the same manner as Fig. 1.

3.4 Computational anticipation of ring-structured $Mn_{18}Bz_{18}^{-/0}$

According to the bottom-up approach presented, the size evolution of the $Mn_nBz_n^-$ clusters was assumed to be terminated at a finite number n, in stark contrast to the linear V–Bz system.[19] Here we computationally anticipate a couple of

ring-structured $Mn_{18}Bz_{18}^{-/0}$, as it was estimated from the extrapolation of the structures **3a**, **4**, and **5** that the cyclization of $Mn_nBz_n^-$ occurs at n = 18. Starting from a C_{18h} geometry, $Mn_{18}Bz_{18}^{-/0}$ were optimized as given in Fig. 5a (details are summarized in Table S7 in the ESI†). Surprisingly, the neutral $Mn_{18}Bz_{18}$ retains C_{18h} symmetry. The $Mn_{18}Bz_{18}^{-/0}$ adopt extremely high spin states: the anion and neutral take $2S + 1 = 54$ and 55, respectively. In both cases, the calculations on the neighboring spin states found higher energies or even met convergence problems within C_{18h} or C_2 symmetry. In fact, both the spin state and the cohesive energies per $Mn_1(\eta^6\text{-}Bz)_1$ unit of $Mn_{18}Bz_{18}^-$ are very consistent with the extrapolation from those of $Mn_nBz_n^-$ (n = 1–5), as shown in Fig. 5b and Fig. S7, respectively. These findings could suggest synthetic feasibility of the large $Mn_{18}Bz_{18}^{-/0}$ rings *via* possible exothermic aggregations of small $Mn_nBz_n^-$.

Fig. 6a shows the frontier Kohn–Sham (KS) orbitals in the α spin part of the neutral $Mn_{18}Bz_{18}$. The α-HOMO has an extensively delocalized bonding character, and can be divided into contributions from the α-HOMOs of each quartet-state Mn_1Bz_1 unit (inset of Fig. 6a), as if the $Mn_{18}Bz_{18}$ exists as a cluster of the Mn_1Bz_1 clusters. The degenerate α-HOMO−1 and α-HOMO−2, and several other α-valence orbitals (6 sets of degenerate and 1 nondegenerate; see Fig. S8 in the ESI†) are isomorphous to the α-HOMO. Interestingly, each delocalized $Mn_{18}Bz_{18}$ orbital allows us to define the number of its orbital nodes k, analogously to π conjugated hydrocarbon systems. Particularly unusual for $Mn_{18}Bz_{18}$ is that the smaller number of nodes is rather associated with the energetically higher orbital. These characteristics are further highlighted by comparing with the frontier orbitals of [18]annulene ($C_{18}H_{18}$), which has a 18-membered ring structure with 18 π electrons (Fig. 6b and Fig. S9 in the ESI†).[37] An intelligible explanation of such delocalized electron systems can be provided by a simple Hückel model: for cyclic conjugated systems, each molecular orbital energy ε_k is given as

$$\varepsilon_k = \alpha + 2\beta\cos\left(\frac{2\pi}{N}k\right) \quad \left(0 \le k \le \frac{N}{2}\right) \qquad (1)$$

where the Hückel parameters α and β are employed. The number of basis functions N is set to 18 in both cases of $Mn_{18}Bz_{18}$ and $C_{18}H_{18}$, in which fragment (or atomic) orbitals of each Mn_1Bz_1 and C are treated, respectively. To apply this model, KS orbital energies were plotted against k and fit by eqn (1); namely, the plots for the $Mn_{18}Bz_{18}$ α-HOMO and lower-lying isomorphous orbitals are shown in Fig. 6c. The same analysis was done for the $C_{18}H_{18}$ frontier orbitals as plotted in Fig. 4d. From the figure the simple Hückel model can describe the $Mn_{18}Bz_{18}$ plot but claims a positive β which contrasts the conventional cases as demonstrated for $C_{18}H_{18}$.

In the following, we indicate that the positive β of $Mn_{18}Bz_{18}$ originates from its strong intra-atomic exchange interactions within the Mn 3d electrons. Let us recall the definition of the Hückel parameter $\beta = \langle\chi_i|\hat{H}|\chi_j\rangle$, where two fragments (or atoms) having basis functions χ_i and χ_j are next to each other. The Hückel Hamiltonian $\hat{H}$ is composed of the kinetic term and the electrostatic potentials by nuclei and other electrons; as its resonance integral name implies, β is in general not significantly affected by two-electron repulsive interactions (the last term in $\hat{H}$; *i.e.*, $\sum_{i<j}^{N}\frac{1}{r_{ij}}$, where r_{ij} is the distance between two electrons), thus resulting in $\beta < 0$. Therefore the positive β implies significant contributions from the two-electron interactions in the $Mn_{18}Bz_{18}$ frontier orbitals. According to previous studies,[21,38,39] the intra-atomic exchange interactions within the metal 3d orbitals induce localized positive and negative spin densities on each metal atom and benzene molecule, respectively, thus stabilizing the ferromagnetic spin ordering in multiple-decker V_nBz_{n+1}. Indeed, this should be also the case for $Mn_{18}Bz_{18}$ due to a pretty large negative spin density (ρ_s = −0.52) for each Bz and the positive spin density of ρ_s = 3.52 per a Mn atom.

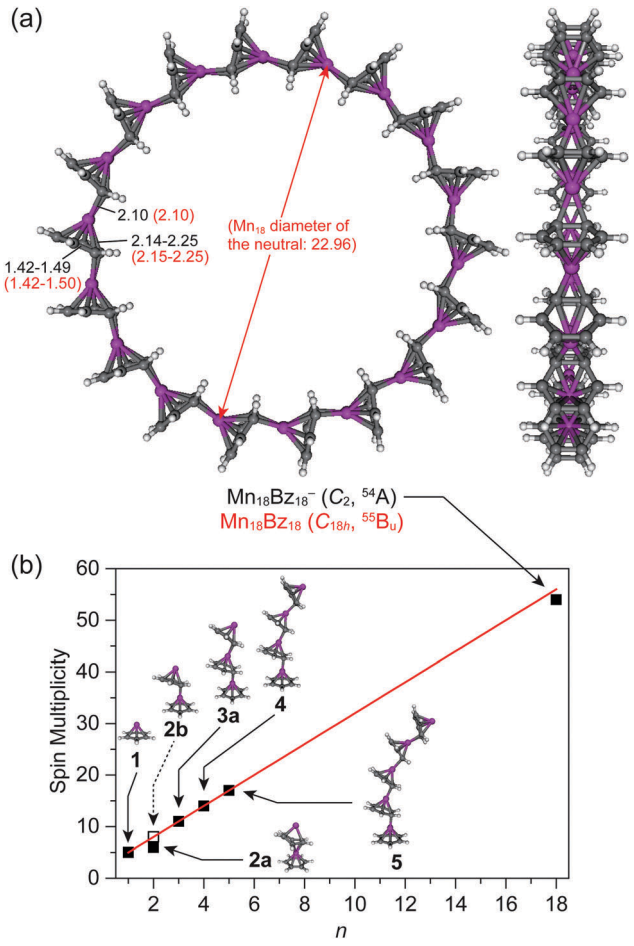

Fig. 5 (a) Top and side views of the optimized structures for $Mn_{18}Bz_{18}^{-/0}$ ring clusters with their symmetries and electronic states. Typical bond lengths are indicated in Å (those of the neutral are given in parentheses). (b) Size-dependent spin multiplicities of $Mn_nBz_n^-$ (n = 1–5 and 18). Because the structure determined for $Mn_2Bz_2^-$ (**2a**) has a different bonding scheme from others, **2b** is explicitly indicated with a white square, even though it is a minor product. The linear extrapolation of the spin multiplicities for tilted multiple-decker sandwich structures is expressed by the red line.

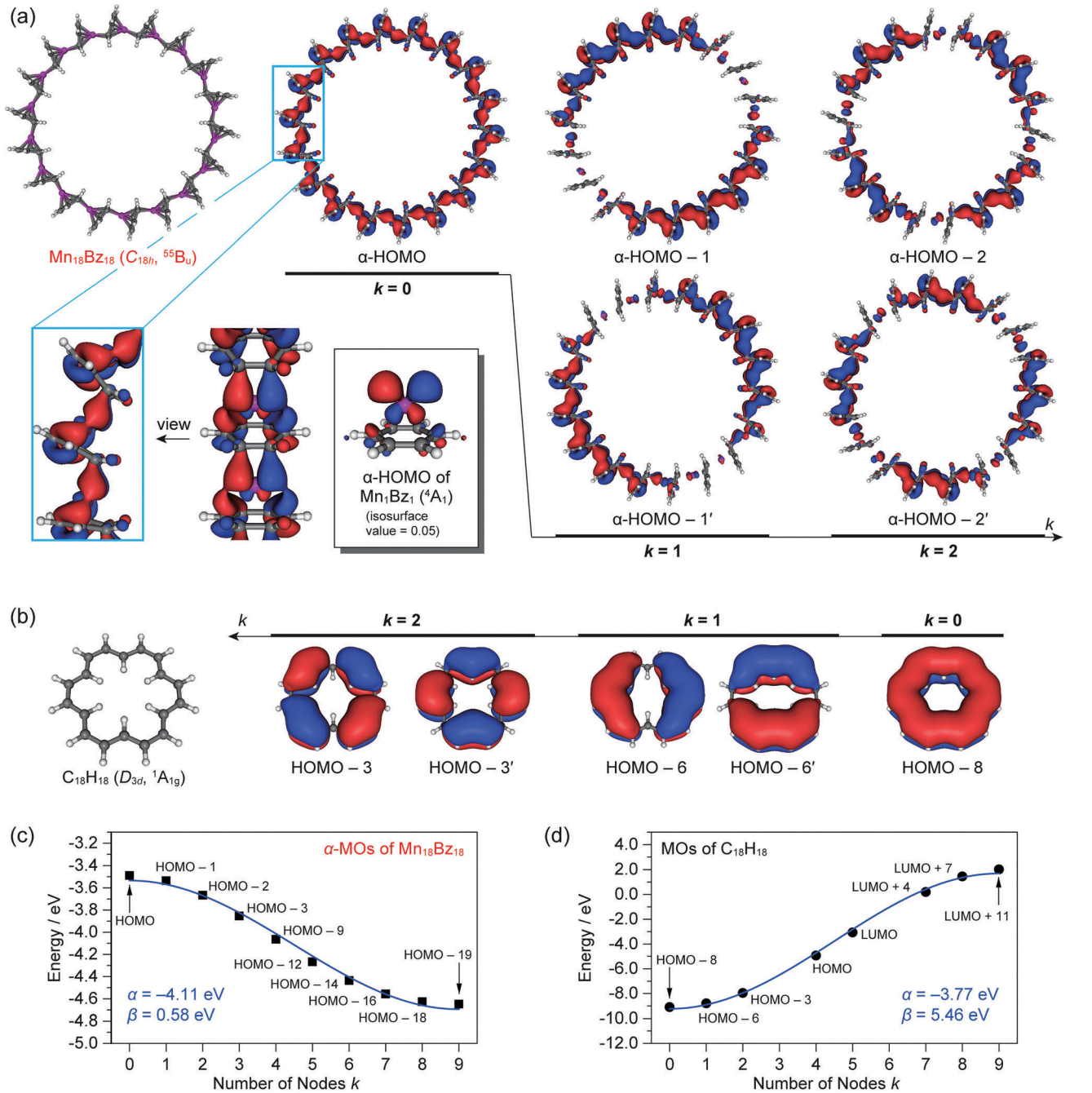

Fig. 6 (a) Frontier Kohn–Sham (KS) orbital pictures in the majority (α) spin part of the $Mn_{18}Bz_{18}$ neutral cluster. The number of nodes k is given for each delocalized orbital. Inset shows top and side views of the partially magnified α-HOMO. The isosurface value of 0.01 was adopted unless otherwise noted. (b) KS orbital pictures of [18]annulene ($C_{18}H_{18}$) with an isosurface value = 0.01, having the same k values as depicted in (a) for comparison. (c) KS orbital energies plotted against k for the $Mn_{18}Bz_{18}$ α-HOMO and lower-lying isomorphous orbitals, and (d) those for the $C_{18}H_{18}$ frontier orbitals composed of delocalized π electrons. Blue lines are obtained by a curve-fitting analysis using eqn (1). Note that two plots for k = 3 and 6 are excluded from (d) because the orbitals are not degenerate under the D_{3d} symmetry of $C_{18}H_{18}$ in our geometry optimization.

3.5 Magnetism of $Mn_{18}Bz_{18}$ in solid-state physics

The periodic nature of $Mn_{18}Bz_{18}$ could allow further discussion on its magnetism from a solid-state point of view. When the aforementioned intra-atomic exchange interactions are restated as the on-site Coulomb repulsion U in the Hubbard model,[40] the $Mn_{18}Bz_{18}$ could be then treated as a $U \gg t$ case (where t is a transfer integral). Despite the high spin state of the $Mn_{18}Bz_{18}$, such $U \gg t$ systems (often referred to as Mott insulators) are believed to usually exhibit an antiferromagnetic ordering of spins.[41] In this sense, the magnetism within the $Mn_{18}Bz_{18}$ cluster might be uncommonly understood from Heisenberg's original picture of ferromagnetism,[42] which is based on Coulomb interactions combined with the Pauli exclusion principle. Interestingly,

several attempts[43,44] have employed the Hubbard model to prove that, in certain lattices, the spin-independent Coulomb interactions can cause a ferromagnetic alignment. Taken together, the low-dimensional and periodic nature of the $Mn_{18}Bz_{18}$ cluster could be therefore exploited as a substantial model for investigating nano-scale magnetism, which allows not only the bottom-up (molecular) but also top-down (solid-state) approaches.

4. Conclusions

We have investigated a series of Mn–Bz cluster anions, $Mn_nBz_n^-$ (n = 1–5), through a joint photoelectron spectroscopic and DFT study. We have shown that $Mn_nBz_n^-$ clusters form multiple-decker sandwich structures with the characteristic tilted Mn–Bz stacking and the high-spin states. Furthermore, a couple of ring-structured $Mn_{18}Bz_{18}^{-/0}$ have been found with the aid of a linear extrapolation from the $Mn_nBz_n^-$ clusters. Importantly, the neutral $Mn_{18}Bz_{18}$ cluster exhibits several striking features, namely, the high symmetry (C_{18h}) structure, the high spin state ($2S + 1 = 55$), and the extensively delocalized electrons.

Lastly, the completely planar (2D) structure of $Mn_{18}Bz_{18}$ at a finite size, when compared to infinite sandwich chain cases, might be advantageous for controlling the cluster's surface morphology (*e.g.*, adsorption states), whose importance in keeping the cluster's functionality has been demonstrated through soft-[45,46] and reactive-landing techniques.[47] We hope that the current work will stimulate synthetic and functionalization efforts on $Mn_{18}Bz_{18}^{-/0}$ as a building block of future SMMs/SCMs.

Acknowledgements

We are grateful to Profs. S. Yabushita (Keio University) and K. Kanoda (The University of Tokyo) for fruitful discussion. We acknowledge Prof. S. Saito (Institute for Molecular Science) and Dr K. Iwahashi (Research Center for Computational Science) for their technical assistance with the computations. This work is partly supported by JSPS KAKENHI of Grant-in-Aids for Scientific Research (A) Grant Number 15H02002. T. M. acknowledges the financial support of Keio Leading-edge Laboratory of Science and Technology (KLL) PhD. Program Research Grant 2015. The computations were performed using Research Center for Computational Science, Okazaki, Japan.

References

1 A. Ardavan, O. Rival, J. J. L. Morton, S. Blundell, A. M. Tyryshkin, G. A. Timco and R. E. P. Winpenny, *Phys. Rev. Lett.*, 2007, **98**, 057201.
2 M. N. Leuenberger and D. Loss, *Nature*, 2001, **410**, 789.
3 M.-H. Jo, J. E. Grose, K. Baheti, M. M. Deshmukh, J. J. Sokol, E. M. Rumberger, D. N. Hendrickson, J. R. Long, H. Park and D. C. Ralph, *Nano Lett.*, 2006, **6**, 2014.
4 L. Bogani and W. Wernsdorfer, *Nat. Mater.*, 2008, **7**, 179.
5 R. Sessoli, D. Gatteschi, A. Caneschi and M. A. Novak, *Nature*, 1993, **365**, 141.
6 D. Gatteschi, R. Sessoli and J. Villain, *Molecular Nanomagnets*, Oxford University Press, New York, 2006.
7 R. Clérac, H. Miyasaka, M. Yamashita and C. Coulon, *J. Am. Chem. Soc.*, 2002, **124**, 12837.
8 W.-X. Zhang, R. Ishikawa, B. Breedlove and M. Yamashita, *RSC Adv.*, 2013, **3**, 3772.
9 G. S. Papaefstathiou, A. Escuer, C. P. Raptopoulou, A. Terzis, S. P. Perlepes and R. Vicente, *Eur. J. Inorg. Chem.*, 2001, 1567.
10 C. Dendrinou-Samara, M. Alexiou, C. M. Zaleski, J. W. Kampf, M. L. Kirk, D. P. Kessissoglou and V. L. Pecoraro, *Angew. Chem., Int. Ed.*, 2003, **42**, 3763.
11 D. E. Freedman, W. H. Harman, T. D. Harris, G. J. Long, C. J. Chang and J. R. Long, *J. Am. Chem. Soc.*, 2010, **132**, 1224.
12 F. Habib, O. R. Luca, V. Vieru, M. Shiddiq, I. Korobkov, S. I. Gorelsky, M. K. Takase, L. F. Chibotaru, S. Hill, R. H. Crabtree and M. Murugesu, *Angew. Chem., Int. Ed.*, 2013, **52**, 11290.
13 M. R. Pederson and S. N. Khanna, *Phys. Rev. B: Condens. Matter Mater. Phys.*, 1999, **60**, 9566.
14 J. Jellinek, P. H. Acioli, J. Garciá-Rodeja, W. Zheng, O. C. Thomas and K. H. Bowen, *Phys. Rev. B*, 2006, **74**, 153401.
15 S. Peredkov, M. Neeb, W. Eberhardt, J. Meyer, M. Tombers, H. Kampschulte and G. Niedner-Schatteburg, *Phys. Rev. Lett.*, 2011, **107**, 233401.
16 V. Zamudio-Bayer, K. Hirsch, A. Langenberg, M. Kossick, A. Ławicki, A. Terasaki, B. v. Issendorff and J. T. Lau, *J. Chem. Phys.*, 2015, **142**, 234301.
17 A. Nakajima and K. Kaya, *J. Phys. Chem. A*, 2000, **104**, 176.
18 A. Nakajima, *Bull. Chem. Soc. Jpn.*, 2013, **86**, 414.
19 K. Hoshino, T. Kurikawa, H. Takeda, A. Nakajima and K. Kaya, *J. Phys. Chem.*, 1995, **99**, 3053.
20 K. Miyajima, A. Nakajima, S. Yabushita, M. B. Knickelbein and K. Kaya, *J. Am. Chem. Soc.*, 2004, **126**, 13202.
21 K. Miyajima, S. Yabushita, M. B. Knickelbein and A. Nakajima, *J. Am. Chem. Soc.*, 2007, **129**, 8473.
22 V. V. Maslyuk, A. Bagrets, V. Meded, A. Arnold, F. Evers, M. Brandbyge, T. Bredow and I. Mertig, *Phys. Rev. Lett.*, 2006, **97**, 097201.
23 H. Xiang, J. Yang, J. G. Hou and Q. Zhu, *J. Am. Chem. Soc.*, 2006, **128**, 2310.
24 Y. Mokrousov, N. Atodiresei, G. Bihlmayer, S. Heinze and S. Blügel, *Nanotechnology*, 2007, **18**, 495402.
25 H. Weng, T. Ozaki and K. Terakura, *J. Phys. Soc. Jpn.*, 2008, **77**, 014301.
26 X. Yao, X. Zhang and J. Wang, *Int. J. Quantum Chem.*, 2015, **115**, 607.
27 T. Masubuchi, K. Ohi, T. Iwasa and A. Nakajima, *J. Chem. Phys.*, 2012, **137**, 224305.
28 T. Masubuchi, T. Iwasa and A. Nakajima, *J. Chem. Phys.*, 2014, **141**, 214304.
29 U. Even, J. Jortner, D. Noy, N. Lavie and C. Cossart-Magos, *J. Chem. Phys.*, 2000, **112**, 8068.
30 J. Perdew, *Phys. Rev. B: Condens. Matter Mater. Phys.*, 1986, **33**, 8822.

31 A. D. Becke, *Phys. Rev. A: At., Mol., Opt. Phys.*, 1988, **38**, 3098.
32 M. J. Frisch, *et al.*, *Gaussian 09, Revision D.01*, (see ESI† for full citation).
33 F. Weigend and R. Ahlrichs, *Phys. Chem. Chem. Phys.*, 2005, **7**, 3297.
34 U. Varetto, *Molekel 5.4.0.8*, Swiss National Supercomputing Centre, Manno, Switzerland, 2009.
35 L. Horváthová, M. Dubecký, L. Mitas and I. Štich, *Phys. Rev. Lett.*, 2012, **109**, 053001.
36 D. N. Shin, Y. Matsuda and E. R. Bernstein, *J. Chem. Phys.*, 2004, **120**, 4150.
37 F. Sondheimer, R. Wolovsky and Y. Amiel, *J. Am. Chem. Soc.*, 1962, **84**, 274.
38 T. Yasuike and S. Yabushita, *J. Phys. Chem. A*, 1999, **103**, 4533.
39 A. Goto and S. Yabushita, *Chem. Phys. Lett.*, 2008, **454**, 382.
40 J. Hubbard, *Proc. R. Soc. A*, 1963, **276**, 238.
41 P. W. Anderson, *Phys. Rev.*, 1959, **115**, 2.
42 W. Heisenberg, *Z. Phys.*, 1928, **49**, 619.
43 A. Mielke, *J. Phys. A: Math. Gen.*, 1991, **24**, 3311.
44 H. Tasaki, *Phys. Rev. Lett.*, 1995, **75**, 4678.
45 S. Nagaoka, T. Matsumoto, E. Okada, M. Mitsui and A. Nakajima, *J. Phys. Chem. B*, 2006, **110**, 16008.
46 S. Nagaoka, T. Matsumoto, K. Ikemoto, M. Mitsui and A. Nakajima, *J. Am. Chem. Soc.*, 2007, **129**, 1528.
47 S. Nagaoka, K. Ikemoto, K. Horiuchi and A. Nakajima, *J. Am. Chem. Soc.*, 2011, **133**, 18719.